Motivation and Objectives

To meet the goal of reducing total U.S. greenhouse gas emissions to 17% below 2005 levels by 2020 and 83% by 2050 [1], and to double the U.S. fuel efficiency standard from 27.3 miles per gallon in 2011 to 54.5 miles per gallon by 2025 [2], advancing lithium-ion battery technology for EVs/PHEVs is of paramount importance. Lithium-ion batteries are currently selected as the energy storage unit for PHEVs/EVs (**Figure 1a**) due to their high energy density (around 150 Wh/kg compared to 50 Wh/kg of Cd-Ni batteries) [3, 4]. The main constituents of a lithium-ion battery include cathode, anode, separator and electrolyte. During charging and discharging, lithium ions extract from and intercalate into nanoscaled cathode materials, accompanied with the transport of electrons through current collector (**Figure 1b**). To provide a better acceleration performance for EVs, a fast and repeatable discharging rate is required. However, capacity loss is found in several conditions: (1) High charging/discharging rate: 23.5% capacity loss while discharging rate increases from 2C to 50C (**Figure 1c**) [4], where the charging/discharging rate of nC represents that the battery is fully charged/discharged in 1/n hour. (2) Long period of cycling: 15.5% capacity loss after 600 cycles at 25˚C is observed [5]. It is commonly thought that diffusion-induced stress is one of the main factors causing loss of capacity in electrode materials. Particle fractures inside electrode materials have been observed after a period of cycling [6-8]. Therefore, there is a fundamental need to provide a mechanistic understanding by considering the structure-mechanics-property interactions.

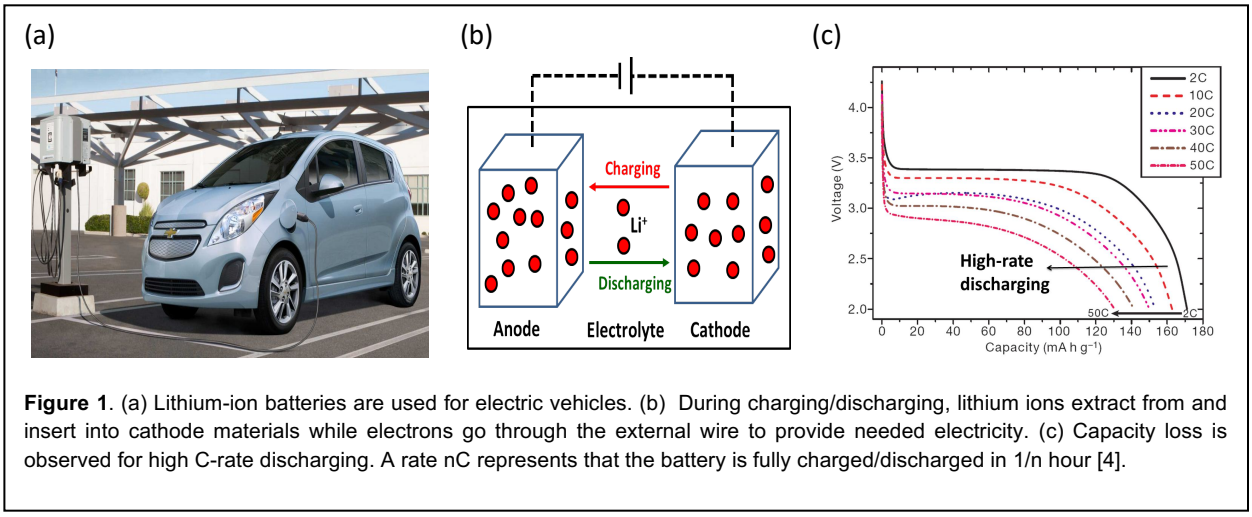

Figure 1. (a) Lithium-ion batteries are used for electric vehicles. (b) During charging/discharging, lithium ions extract from and insert into cathode materials while electrons go through the external wire to provide needed electricity. (c) Capacity loss is observed for high C-rate discharging. A rate nC represents that the battery is fully charged/discharged in 1/n hour [4].

The goal of this proposed work is to investigate the evolution of diffusion induced stress accompanying the solid state phase transformation, and relate the stress generation during the lithiation process to the particle fracture and C-rate dependent capacity loss. Two main objectives will be conducted to achieve this goal:

- **Objective 1**: To investigate the diffusion induced stress with phase change in a single particle by incorporating lithium-concentration-dependent material properties.

- **Objective 2**: To investigate how C-rate affects lithium concentration profiles and stress evolution inside cathode materials.

The results of proposed work will provide a better understanding of generation of diffusion induced stress in electrode materials. The study will incorporate anisotropic material properties, volume misfit and coherent interface during the lithiation process. The simulation model built in this work will be verified and compared with the available experimental observations. All in all, the proposed work will contribute to our fundamental knowledge of interplay between lithium intercalation, stress evolution, particle fracture and capacity fade in lithium-ion batteries.

Background and Significance

a) The importance of advanced energy storage systems

Decreasing the dependence on foreign oil is critical for national economy and security for the Unite States. Today, the United States imports 50-60% of the total oil consumption in which transportation sector accounts for nearly 72% [9, 10]. Therefore, the development of PHEVs/EVs plays an important role in reducing both the petroleum consumption and greenhouse gas emissions. Batteries with higher capacities and capabilities of high rate charging/discharging are needed to stimulate the popularity of PHEVs/EVs.

b) Current state-of-the-art

Among the many cathode materials, the olivine-based lithium-iron-phosphate ($LiFePO_4$) with an orthorhombic crystal structure provides excellent characteristics for application in EVs/PHEVs such as: good thermal stability, abundant iron resource, low raw material cost, and high theoretical energy density (170 mAh/g) [11]. However, electronic conductivity and diffusivity for $LiFePO_4$ are considerably lower than those of $LiMn_2O_4$ and $LiCoO_2$ materials [12], and these intrinsic disadvantages of $LiFePO_4$ are currently improved by doping, carbon coating, nano-scale particle size, or synthesis controls [11, 13-15]. It has been reported that the electrochemically cycled $LiFePO_4$ under low C-rate exhibits as a two-phase system [16-19]: lithium-rich ($LiFePO_4$) and lithium-poor ($FePO_4$) phases with a flat voltage response. The two phases have similar crystal structures and are constrained by a coherent interface during the phase transformation [20]. Because of different lattice constants for the two phases, approximately 6-7% volume misfits are observed (**Figure 2a**) [18, 21]. Moreover, computational simulations and experimental observations have identified that lithium ion diffusion in $LiFePO_4$ is one-dimensional and confined along the b-axis (**Figure 2b**) [22-26]. Chen et al.[6] have studied the phase boundary via high resolution transmission electron microscopy, and cracks on bc plane (**Figure 3**) were observed on the particle surface and this might be caused by the coherent strain between two phases.

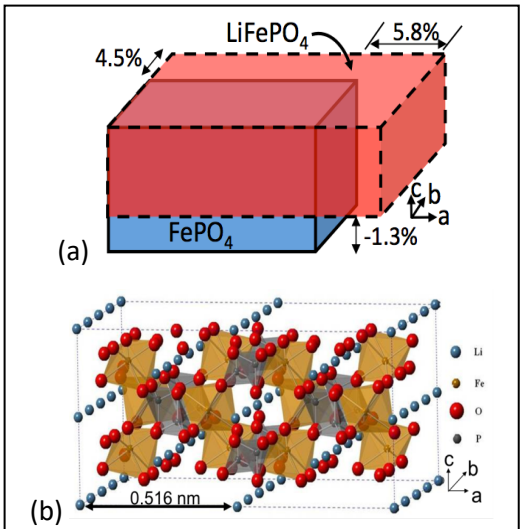

Figure 2. (a) Volume change occurs during the phase transformation from $FePO_4$ to $LiFePO_4$ phases (5.8% and 4.5% expansion in the a and b-axis, and 1.3% contraction in the c-axis). (b) One dimensional lithium diffusion along the b-axis in $LiFePO_4$.

On the other hand, Laffont et al.[27] have reported a nano-sized interfacial zone (ca. 8-22 nm) between two single phases, and it is always found in a partially lithiated/delithiated particle with sizes ranging from 130 to 172 nm. It is concluded that for the low C-rate cases, the phase boundary tends to move along the a-axis with the extension of the pre-existing phase. Later, Delmas et al.[28] proposed a domino-cascade model (**Figure 4**) to explain the intercalation/extraction of lithium ions in a single particle based on the assumption that a mixture of particles in a discharging sample are either fully lithiated or delithiated. It is suggested that the phase boundary propagation wave along the a-axis is formed because of the relatively low energy barrier in the distorted interfacial area. The model was later confirmed experimentally by Brunetti et al.[29], showing that most particles ranging from 50 nm to 300 nm in a partially charged lithium-ion cell sample are either in a fully $LiFePO_4$ phase or a $FePO_4$ phase. Meethong et al.[18] and Tang et al.[30, 31] discussed the role of the coherency-induced elastic energy during the phase transformation by incorporating spherical particles. Van der Ven et al.[32] studied the role of coherent strains on the phase stability of needle crystallites and it was concluded that the minimum strain energy could be maintained by decreasing the interfacial area on the bc-plane between two phases.

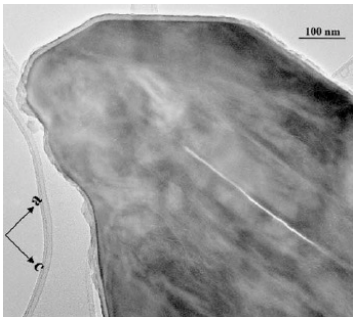

Figure 3. TEM image showing the crack in the bc plane was observed on the particle surface [6].

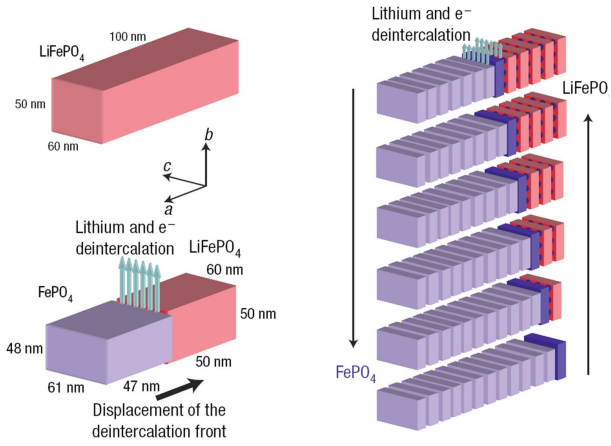

Figure 4. Schematic illustration of the domino-cascade mechanism during lithiation/delithiation in a $LiFePO_4$ crystallite [28].

Various studies have been devoted to investigate the phase transformation path of $LiFePO_4$ under high C-rate [19, 33, 34]. Bai et al [33]. proposed a model to relate the voltage response and phase transformation path for a single particle. The results indicates that when C-rate reaches a critical value, two phase separation behavior observed in low C-rate will be suppressed (**Figure 5**), and replaced by a solid solution phase transformation pathway.

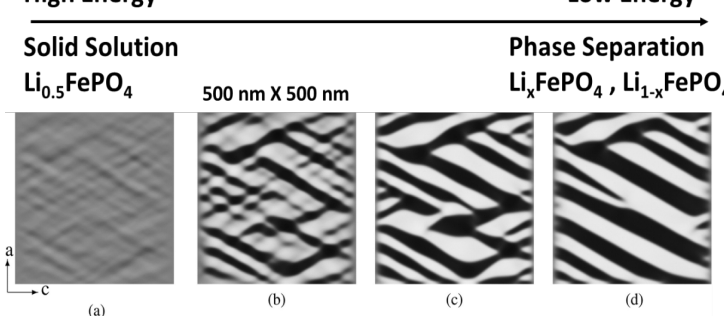

Figure 5. Suppression of phase separation inside materials for high C-rates. From (a) to (d) showing the phase separation over time when the battery is discharged to $Li_{0.5}FePO_4$ under high C-rate. The composition will change from a higher energy state to a lower energy state [33].

Despite the collective studies, it is absolutely necessary and timely to investigate the diffusion-

induced stresses in $LiFePO_4$ as a whole: the anisotropic directions of the diffusion and the phase boundary movement should be incorporated, and the concentration-dependency of anisotropic material properties and volume expansions should be considered. The results of this proposed work could be used as a tool to provide a better understanding of mechanisms of lithium ion diffusion, stresses on the phase boundary, fracture propensity, and C-rate dependent capacity loss.

Preliminary Studies

a) C-rate dependent voltage response

It has been reported that lithium diffusion mechanism and phase transformation path might be C-rate dependent [19, 33, 34]. This will lead to a different stress formation inside materials. To compare the lithium intensities between different C-rates, we first conduct the charging/discharging experiment (1C, 2C, 6C and 10C). Commercial 26650 cylindrical $LiFePO_4$ lithium ion batteries with a capacity of 2.5Ah (**Figure 6a)** are used in the previous study. The charging/discharging experiments are conducted via an Arbin BT2000 cycler (Arbin Instrument, College Station, TX) which is located at North Carolina State University (**Figure 6b)**. By referring to the experimental protocol of the automotive application batteries [5], the following steps are used to conduct the charging/discharging experiment: (1) Galvanostatically charge to 3.6V at constant current I=2.5A, (2) convert to potentialstatic charging at constant voltage V= 3.6V until the current drops to C/20 (0.125A). The purpose of this step is to ensure the battery is fully charged. (3) discharge the batteries at different C-rates until the voltage drops to the recommended lower bound of the working voltage (2V), and (4) galvanostatically charge the batter at different C-rates to 3.6V. The steps (1) to (4) are repeated three times in order to ensure that a repeatable voltage-time curve is obtained.

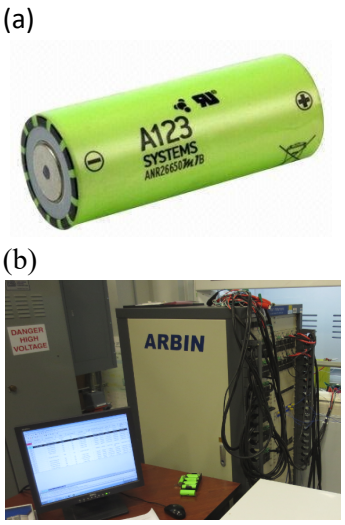

Figure 6. (a) Commercial 26650 $LiFePO_4$ batteries. (b) Arbin BT 2000 cycler for the charging/discharging experiment.

The results are shown in **Figure 7**. The hysteresis (charging and discharging have different voltage responses) between charging and discharging curves for all C-rates are observed. The voltage gap (between charging and discharging) increases with an increasing C-rate. For example, considering the location of the capacity = 0.015 (Ah/g), the voltage gaps are approximately 0.18 (V), 0.25 (V), 0.45 (V), and 0.68 (V) for 1C, 2C, 6C and 10C, respectively (**Figure 7**). The trend of these quantitative data is consistent with the observation in ref [35]. Besides, due to the characteristic of the two-phase system for $LiFePO_4$ material, flat voltage curves are noticed between the capacity of 0.005 and 0.025 (Ah/g) for all C-rates. However, by comparing the voltages of discharging curves in the millivolt scale, the voltage curves in this section are not perfectly horizontal, as shown in the inset of **Figure 7**. An increasing dropping-slope of the curves is observed with higher C-rate, and a stronger voltage fluctuation for the 10C sample is noticed, suggesting that an extra over-potential is required to overcome the energy

barrier during the phase transformation of $LiFePO_4$ [32, 36, 37]. Due to a higher driving force for the high C-rate sample, lithium ions could possibly insert into multiple particles at the same time [35]. Thus, compare to the low C-rates, the observation of the voltage fluctuation in 10C might lead to a: (1) Different lithium insertion mechanism (2) different lithium intensity depth profile and (3) different lithium-ion distribution.

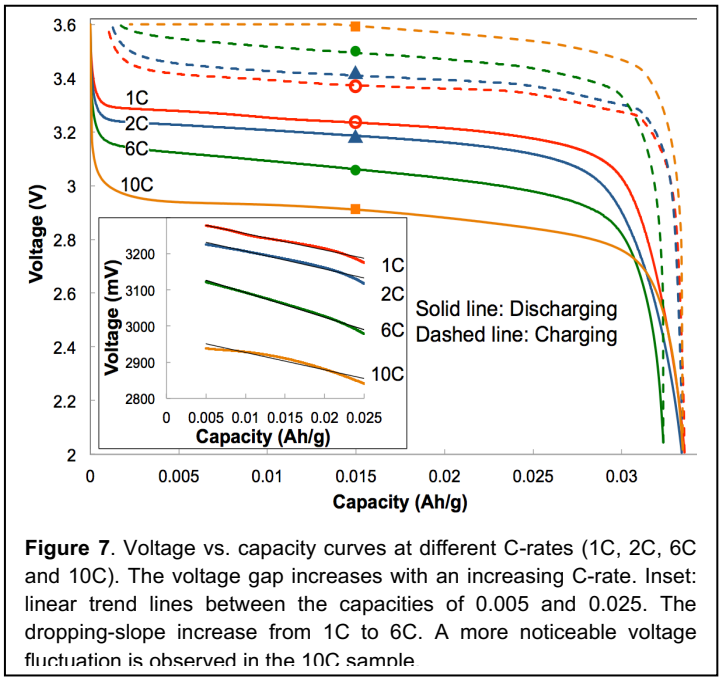

Figure 7. Voltage vs. capacity curves at different C-rates (1C, 2C, 6C and 10C). The voltage gap increases with an increasing C-rate. Inset: linear trend lines between the capacities of 0.005 and 0.025. The dropping-slope increase from 1C to 6C. A more noticeable voltage fluctuation is observed in the 10C sample

b) Lithium-ion intensity detection

To directly detect the lithium intensity, Time-of-Flight Secondary Ion Mass Spectrometry (ToF-SIMS) is selected as the analysis tool. ToF-SIMS is a highly sensitive surface analytical technique that can be used to detect atoms and molecules even at low concentration down to ppm level [38]. The sample surface is bombard by a high energy (~25 keV) primary ion beams (e.g. Bi_3^+). The emitted secondary ions from the sample will be then analyzed by calculating the flight time required to travel from the surface to the detector. A mass spectrum could be thus derived to reveal the surface chemical composition (**Figure 8**). The acquisition of intensity depth profile by using ToF-SIMS is destructive due to the removal of sample material during the analysis. **Figure 9** shows the sample surface before and after sputtering. The crater size generated by Cs^+ ion beam is 80 μm x 80 μm to avoid crater effect and the actual analyzed area is 10 μm x 10 μm in the middle of the removed material.

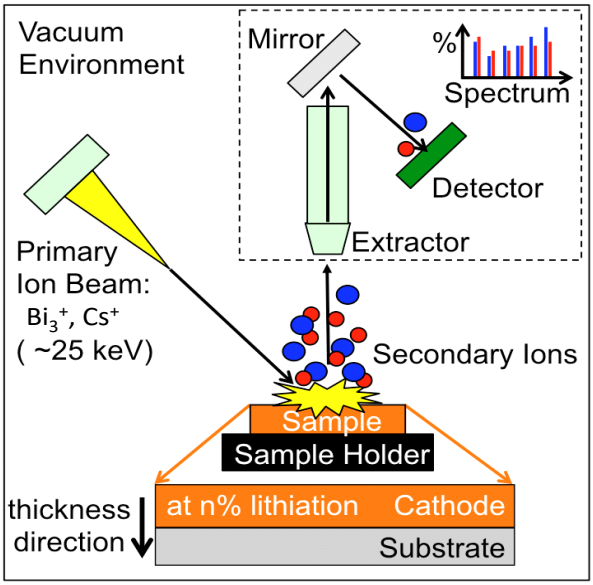

Figure 8. A schematic depiction of ToF-SIMS. The primary ion beams(Cs^+, Bi_3^+) with energy in the keV range impinge upon the sample which is mounted on a holder, causing the emission of the secondary ions. The time required for atoms/molecules to hit the mass detector will be calculated and the spectra of mass to charge (m/z) ratio could be derived.

The cells are first fully discharged to 0 Volt then disassembled with long $LiFePO_4$ stripes are unrolled in a MBRAUN MB20G glove box system (M. Braun Inertgas-Systeme GmbH, Stratham, Germany) filled with nitrogen atmosphere to avoid the effect of air exposure [39]. The oxygen level in the glove box is maintained down to 1 ppm. For each cell we choose two different locations on the unrolled cathode material for the ToF-SIMS analysis (2 cells for each C-rate). ToF-SIMS analyses in

this study are conducted by using an ION TOF ToF-SIMS V (ION TOF, Inc. Chestnut Ridge, NY) instrument equipped with a Bi_n^{m+} (n = 1−5, m = 1,2) liquid metal ion gun and a Cs^+ sputtering ion gun. Both the Bi and Cs ion columns are oriented at 45° with respect to the sample surface normal. The instrument vacuum system consists of a load lock for rapid sample loading connected by a gate valve to the analysis chamber. The analysis chamber pressure is maintained at or below 5.0 x 10^{-9} mbar to avoid contamination of the surfaces to be analyzed.

The experimental results shown in **Figure 10** indicate that: (1) Fully discharged commercialized cells provide homogeneous Li-ion distribution at various C-rates (**Figure 10a).** Only the sample #3 of 6C is shown here. (2) fully discharged commercialized cells provide almost equivalent Li^+/Fe^+ counts at various C-rates (**Figure 10b)**. During the charging/discharging process, lithium ions are inserted and extracted from cathode materials while iron atoms remain inside the crystal [40]. Thus the intensity of Fe^+ is used as a baseline to compare with the lithium intensities for different samples. It could also be observed that Fe^+ are distributed homogeneously inside the material (**Figure 10 a).**

From these data, we speculate that the voltage fluctuation in high C-rate is only related to a different lithium insertion mechanism, not lithium intensity. When the particles are fully discharged, the total lithium intensity inside material should be C-rate independent. The layer-by-layer lithium intercalation process for low C-rate cannot be used to describe the lithiation process for high C-rate. Thus, a comparison of stress evolution between low C-rate and high C-rate mechanism is important to help understand the capacity loss inside materials.

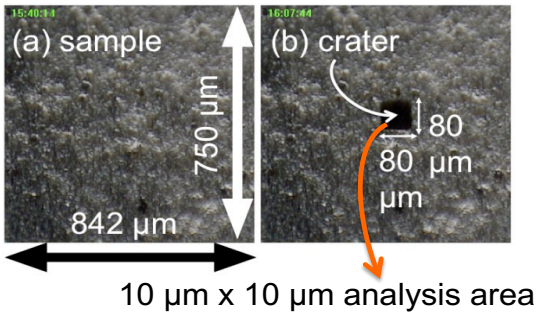

Figure 9. Images of the sample surface (a) before and (b) after the sputtering process. The crater size is 80 x 80 µm, and the analysis area is 10 x 10 µm in the middle of the sample to avoid the crater effects.

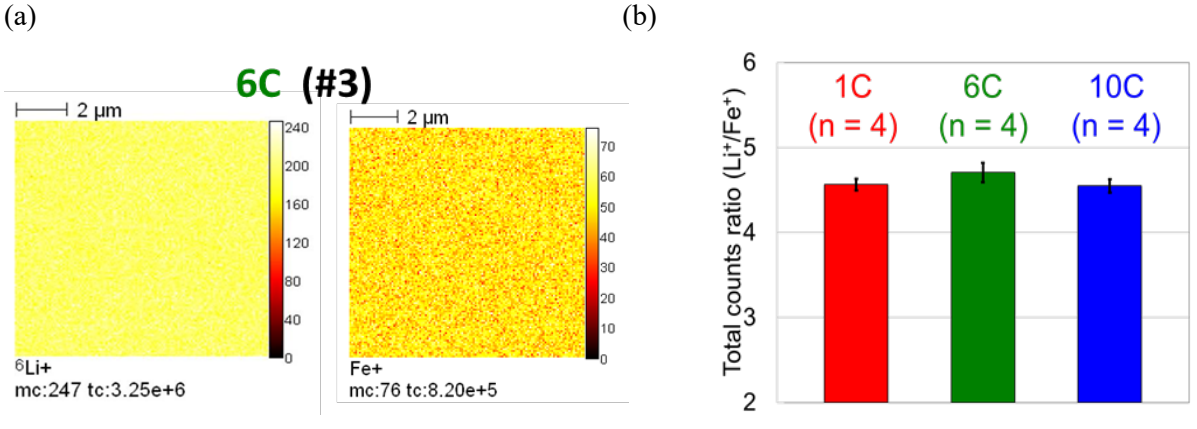

Figure 10. (a) Total counts of lithium and iron for one 6C sample. A 10 x 10 µm area is analyzed and the resolution is 128 x 128 pixels. The result shows a homogeneous distribution in the sample. Mc represents the maximum count (intensity) at a specific pixel and tc is the sum over all intensities of pixels (b) Ratios of total counts of Li^+/Fe^+. The samples for 1C, 6C and 10C do not show a significant difference.

Research Design and Methods

Objective 1: To investigate the diffusion induced stress with phase change in a single particle by incorporating lithium-concentration-dependent material properties.

Rationale:

It is commonly thought that diffusion-induced stress is one of the main factors causing loss of capacity in electrode materials. Particle surface fractures inside electrode materials have been observed after a period of cycling [6, 40]. During discharging, lithium ions intercalate into $LiFePO_4$ cathode materials and result in concentration variations along the material thickness. For Li_xFePO_4 material, lithium concentration (x) varies between two single phases, $FePO_4$ (x=0) and $LiFePO_4$ (x=1), and anisotropic volume expansion occurs during lithium intercalation due to different lattice constants of two single phases. Previous studies have shown that during the lithium intercalation process for low C-rate, the phase boundary lies in the bc plane and propagates along the a-axis [6, 27]. Traditional core-shell model (spherical particle) is not suitable for the stress prediction for $LiFePO_4$ material because the model assumes: (1) The phase boundary moves in the radial direction and (2) isotropic material property. These assumptions are inconsistent with the low C-rate $LiFePO_4$ behavior. Therefore, in **objective 1** we use a single plate-like $LiFePO_4$ particle incorporating anisotropic properties as our model system to investigate the mechanical stress evolution, specifically on the phase boundary during the lithiation process.

Research Plan:

Task 1.1 Stress evolution on the phase boundary

Our previous work utilized a thermal stress analysis approach to investigate the stress evolution during the lithium intercalation process in a single particle [41]. ANSYS finite element software (ANSYS, Inc., Canonsburg, Pennsylvania, USA) is incorporated and a plate-like $LiFePO_4$ single particle with dimensions of 150 nm x 60 nm x 100 nm is developed (**Figure 11**); the particle size is designed to be within the range of experimental observation [27-29]. The thermal diffusivity mimics the lithium-ion diffusivity, and the temperature gradient represents the lithium-ion concentration gradient.

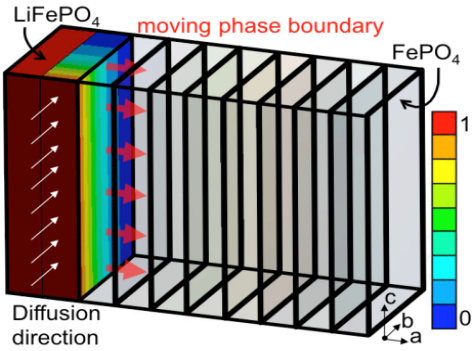

Figure 11. A plate-like Li_xFePO_4 single particle finite element model with a dimension of 150 nm x 60 nm x 100 nm, where lithium ions diffuse along the b-axis and the phase boundary moves along the a-axis. The model is divided into 10 layers along the a-axis, and each layer represents one lithium ion diffusion channel. Colored legend: High lithium ion concentration is in red and low lithium ion concentration is in blue.

To simulate the lithium diffusion along the b-axis while the phase boundary propagating along the a-axis, the finite element model containing 3780 elements is divided into 10 layers along the a-axis and each layer represents one lithium-ion diffusion channel (**Figure 11**), whereas each channel contains 378 elements along the b-axis. A 10-step finite element analysis is designed, such that each step represents diffusion in each channel. As shown in **Figure 11**, one channel must be fully filled with lithium before intercalating into the adjacent channel. This model

meets two main characteristics for low C-rate lithiation process: (1) One dimensional diffusion along the b-axis [22, 23, 25, 26, 37]. (2) The phase boundary between $FePO_4$ and $LiFePO_4$ phases lie in the bc plane [6, 27].

Moreover, it has been indicated that the change of the material properties during lithiation will affect the stress generation. Specifically, the material stiffening is beneficial for avoiding surface cracking [42]. For $LiFePO_4$, material properties should vary between two single phases ($FePO_4$ and $LiFePO_4$) during the lithiation process. In our model, concentration-dependent anisotropic material properties and volume expansions for Li_xFePO_4 are incorporated: anisotropic material property matrices [C] and the volume expansion (α) are defined as follows: $[C(x)] = x[C]^{LiFePO_4} + (1-x)[C]^{FePO_4}$ and $\alpha_i(x) = x\alpha_i^{LiFePO_4}$, where i = a, b, and c representing lattice vectors. Orthorhombic elastic constants as shown in **Table 1** for both the lithium-rich and lithium-poor phases are obtained from the reference [43]. The anisotropic volume expansions of the $LiFePO_4$ phases are obtained from the literature, in which α_a=5.8%, α_b =4.5%, and α_c =-1.3% [17, 21]. The anisotropic diffusion-controlled analysis requires a set of boundary and initial conditions for each channel: a unit of concentration on one surface Φ(y, t) = Φ(0, t) = 1, and a zero-concentration on the other surface at the end of the said channel Φ(y, t) = Φ(1, 0) = 0 (**Figure 11**), where Φ is the concentration, y is the diffusion length along the b-axis, and t is the time required for the completion of the diffusion. The time-dependent concentration gradient serves as the driving force of the diffusion for the phase transformation [44-46], and it is described by the governing equation: $\frac{\partial \phi}{\partial t} = D\left(\frac{\partial^2 \phi}{\partial y^2}\right)$. That is, the Fick's second law of diffusion, where D is the diffusivity. The concentration–independent diffusivity along the b-axis is defined as D_b = 1E-15 m^2/s obtaining from Park et al [12]. Since studies have shown that lithium-ion hopping between channels is very unlikely [47], and to ensure the anisotropic diffusivity, the diffusivities of the other two directions are set to be 10-order of magnitude smaller comparing to the one along the b-axis: $D_a = D_c$ = 1E-25 m^2/s. It is to ensure that lithium ions move smoothly and systematically from high-concentration regions (in red) to low-concentration regions (in blue) within channels (**Figure 11**).

Table 1. Elastic constants calculated from first principles for $FePO_4$ and $LiFePO_4$ phases [43].

Phase	Volume ($Å^3$)	Lattice constants (Å)			Elastic constants (GPa)								
	V	a	b	c	C_{11}	C_{22}	C_{33}	C_{44}	C_{55}	C_{66}	C_{12}	C_{13}	C_{23}
$FePO_4$	284.57	9.96	5.88	4.86	175.9	153.6	135.0	38.8	47.5	55.6	29.6	54.0	16.6
$LiFePO_4$	299.54	10.45	6.05	4.74	138.9	198.0	173.0	36.8	50.6	47.6	72.8	52.5	45.8

The stress field on the phase boundary at different percentages of lithiation is studied. The simulation results are shown in **Figure 12** and **Figure 13**. Normal stress σ_{xx} and shear stresses σ_{xy} and σ_{xz} on the phase boundary are at their highest values on the free surfaces of the phase

boundary (**Figure 12**). These diffusion-induced stresses could possibly lead to the occurrence of Mode I, Mode II, and Mode III fractures if an initial crack exists on the ac-plane (**Figure 13**).

The plot shows the stress distribution on the phase boundary under different lithiation stages. Concentration-dependent normal stresses σ_{xx} are observed, and these are due to molar volume misfits since two phases are constrained at a coherent interface (**Figure 12a-f**). It is also observed that the particle is in compression (σ_{xx}) at the low lithiation stage (**Figure 12a-c**) and is in tension beyond 50% lithiation (**Figure 12d-f** and **Figure 13a**). Our study also shows that when the particle is toward fully lithiated (90%), larger tension occurs on the free surface parallel to the z-axis (**Figures 12f and 13a**), suggesting a crack opening might occur if an initial flaw exists on the ac-plane. The lithiation causes non-negligible shear stress σ_{xy}, specifically along the particle free-surfaces (**Figures 12g-l and 13c**), suggesting that such high shears could be responsible for the observed surface cracking (**Figure 13c-d**) [6, 8]. It is observed that σ_{xy} increases when lithiating to 50% (**Figure 12g-j**), and the shearing stress starts decreasing beyond 50% lithiation (**Figures 12j-l and 13c**). This indicates that $LiFePO_4$ particles are subjected to the highest diffusion-induced shear stresses at the 50% lithiation stage. Furthermore, lithiation-independent σ_{xz} are uniformly distributed on the phase boundary (**Figures 12m-r and 13e**). The shear stresses are observed with larger values at corners close to the free surfaces, indicating these locations are susceptible to fracture (**Figure 12e-f**). Comparing stress magnitudes at 50% lithiation, $\sigma_{xx} : \sigma_{xy} : \sigma_{xz} = 1:3:1$, the result indicates that Mode II fracture is more likely to occur before other two modes. Taking together, this result provides a connection between diffusion-induced stresses at the phase boundary and the cracking propensity on the ac-plane.

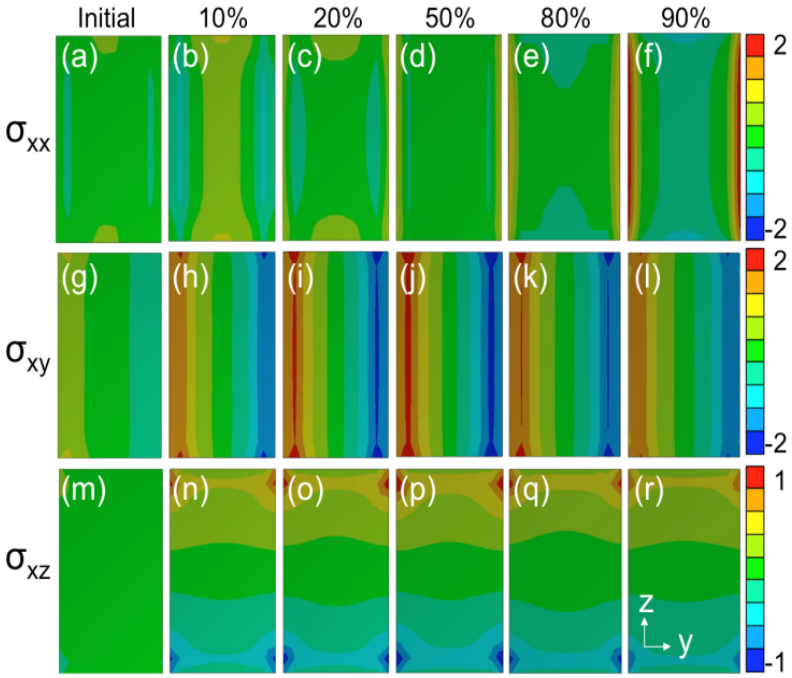

Figure 12. A representative normalized stress field on phase boundaries at different lithiation stages for the low C-rate model. (a)-(f): the particle is in compression (σ_{xx}) at low lithiation stages and in tension at high lithiation stages. This is due to the volume misfit of the two phases and the coherent interface. (g)-(l) High in-plane shear stresses (σ_{xy}) along the particle surfaces are observed, and the results suggest that

particles are subjected to the highest σ_{xy} at 50% lithiation. (m)-(r): Lithiation-independent in-plane shear stresses σ_{xz} are uniformly distributed on the phase boundary and corners are subjected to higher mechanical stresses. Colored legend: Tension is in red and compression is in blue.

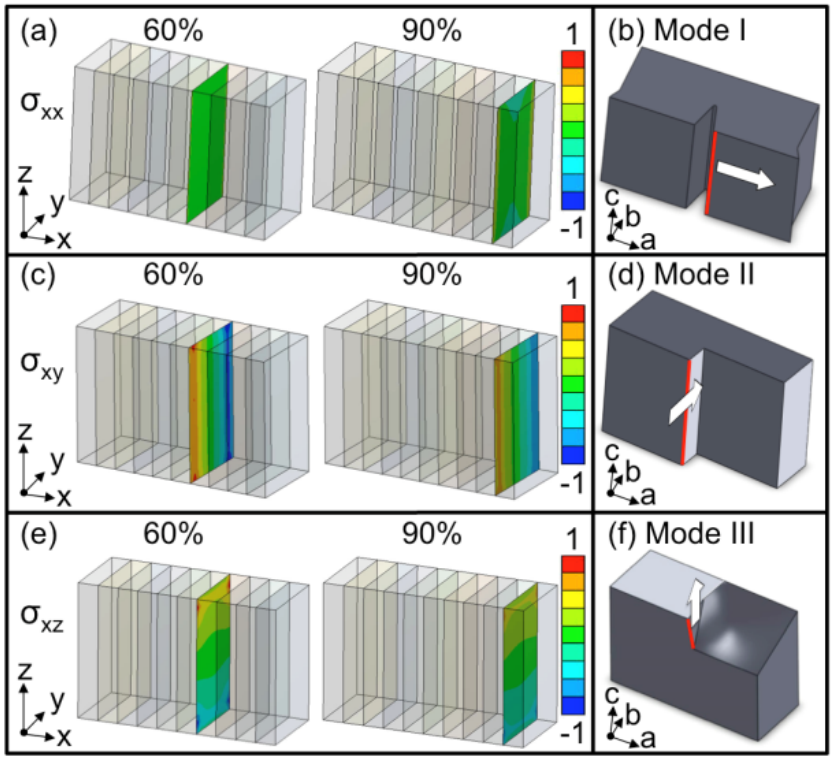

Figure 13. A representative normalized stress field on the phase boundary at different lithiation stages for the low C-rate model. An initial crack at the surface of the particle under repetitive (dis)charging cycles could lead to Modes I, II, and III fractures. (a)-(b) When the particle is more than 60% lithiated, larger σ_{xx} tension exists on the free surface parallel to the z-axis, suggesting that a Mode I fracture might occur if an initial flaw (presented in color red) exists on the ac-plane. (c)-(d) Large σ_{xy} exists on the yz-plane parallel to the phase boundary, suggesting that a Mode II fracture could occur. (e)-(f) Lithiation-independent σ_{xz} on the phase boundary could lead to a Mode III fracture. Colored legend: Tension is in red and compression is in blue.

Task 1.2 Comparisons of strain energy evolution between different C-rates

The single particle model could also be extended to investigate the C-rate dependent strain energy evolution during lithiation as shown in **Figure 14**. The 1C model (layer-by-layer phase transformation) is as described in task 1.1 and is inspired by Delmas et al.[28]. High C-rate finite element models utilize the approach proposed by Singh et al [48] based on the concept that the number of the phase boundary is proportional to the C-rate. It could be observed that the local maximum strain energy is reached when a phase boundary is fully formed. The reduction of the complete phase boundary results in the relaxation of the strain energy thus causes a saw-like shape in the strain energy curve. The strain energy of the particle with 40% lithiation at different C-rates is also compared, as indicated by square markers (**Figure 14**). The result shows that with the same amount of lithiation, particles experience different strain energies at different C-rate discharging. It could be expected that 1C model should have lowest strain energy since

only one phase boundary existed during lithiation. The high elastic energy from the 6C model suggests that the existence of multiple coherent interfaces within a particle could be unstable and require a higher driving force (i.e. higher C-rate) to overcome the energy barrier.

Upon completion of the **Objective 1**, we could provide quantitative date for diffusion induced stress inside a single particle, and relate the stress components to different fracture modes. The variation of the strain energy during lithiation via different phase transformation path could be used to explain why a layer-by-layer lithium diffusion mechanism is more favored for low C-rate.

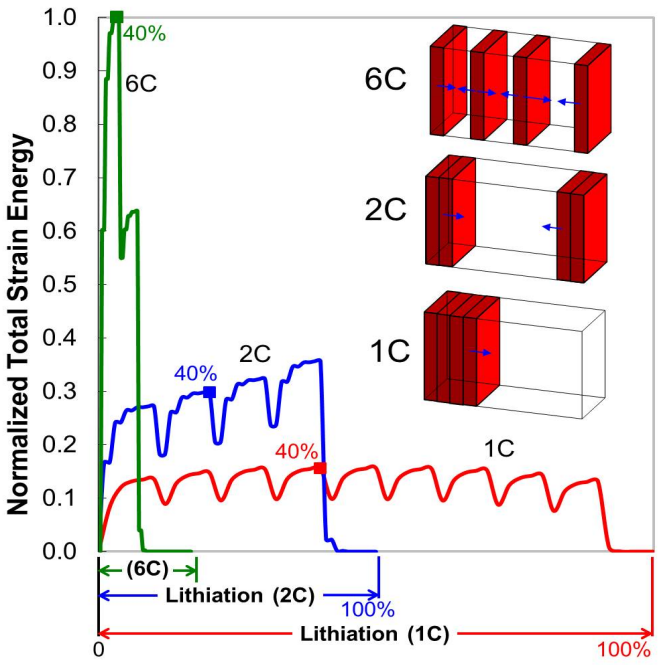

Figure 14. The C-rate dependent strain energy evolution during a complete lithiation cycle. The strain energies in the particles with 40% lithiation are indicated by square markers. The 1C model uses a sequential phase transformation path proposed by Delmas et al.[28] and high C-rate models are inspired by Singh et al.[48]. The high elastic energy from the 6C model suggests that the existence of multiple coherent interfaces within a particle could be unstable, and therefore Singh's approach is not plausible thermodynamically. As a result, lithium ion diffusion in multiple channels or in the ac-plane simultaneously are more plausible for the high C-rate model.

Objective 2: To investigate how C-rate affects lithium concentration distributions and stress evolution inside cathode materials.

Rationale:

Several studies have shown that for fast (dis)charging, $LiFePO_4$ material does not demonstrate a two-phase system [4]. Thus, the phase transformation path for higher C-rates is considered to be different compared with the layer-by-layer phase transformation path for low C-rates. Another phase transformation path is more likely to happen: a homogeneous phase transformation accompanying the suppression of two-phase separation in $LiFePO_4$ particles as discussed by Bazant [33, 34] although the phase separation might occur when the overpotential is removed (**Figure 5**). Our preliminary study also shows that at high C-rate, the fluctuation in the voltage response (10C) could be observed (**Figure 7**). For the cases of higher C-rates, higher lithium ion mass fluxes pass through the material surface [49]. When the particles are fully discharged, the total lithium intensity inside material should be C-rate independent as shown in our previous study (**Figure 10**). However, different mass fluxes will cause different time histories of lithium concentration variation accompanied with the phase transformation and stress evolution. It is commonly considered that higher C-rates result in higher internal stresses, causing the particle fracture and capacity loss after a period of cycling [7]. In **Objective 2,** we aim to investigate how C-rate affects lithium concentration growth and stress evolution inside a multi-particle cathode system from a macroscopic point of view. The results from **Objective 2** will provide insights into how

anisotropic volume misfit, intrinsic $FePO_4$ and $LiFePO_4$ orthorhombic material properties, and lithium concentration variation under different C-rates affect stress formation inside cathode materials.

Research Plan:

To simulate lithium intercalation process under different C-rates, we again adapt a thermal stress analysis approach. The Fourier law (heat flux $q = -k\frac{\partial T}{\partial y}$) is used to simulate different mass fluxes described by the Fick's law (mass flux $J = -D\frac{\partial \Phi}{\partial y}$), where k is thermal conductivity and D is diffusivity. The heat flux (w/m^2) mimics the mass flux (mass/m^2) of lithium ions and the temperate gradient represents the lithium concentration gradient. A thermal–static stress coupling finite element model is adapted to investigate stress evolution under different C-rates (1C, 2C, 6C and 10C). As mentioned in **Objective 1**, the concentration-dependent anisotropic properties is defined between x=0 and x=1 in our model system. The maximum concentration needs to be confined to be 1 in order to incorporate this assumption into the high C-rate model. Thus the analysis is divided into two steps (**Figure 15**): (1) In step one, lithium ions are pumped into the material via different mass fluxes (1C=0.022 W/m^2 in our model system) (**Figure 15a**). The direction of the mass flux is assumed to be aligned with the direction of the lithium diffusion (b-axis). The time required for surface lithium concentration to reach stoichiometric maximum varies with different mass fluxes, i.e. different C-rates. Once the concentration on the surface reaches 1, the simulation process will switch to step 2. (2) In step two, the boundary condition of a fixed mass flux will be replaced by a fixed concentration (C=1) on the surface. The simulation continues till the material is fully lithiated (**Figure 15b**). Large deformation will be incorporated in the model in order to be applied for other material systems. The selected time histories of the lithium concentration for different C-rates will be imported into static analysis module to calculate the corresponding stress and strain energy evolution during the lithium intercalation process.

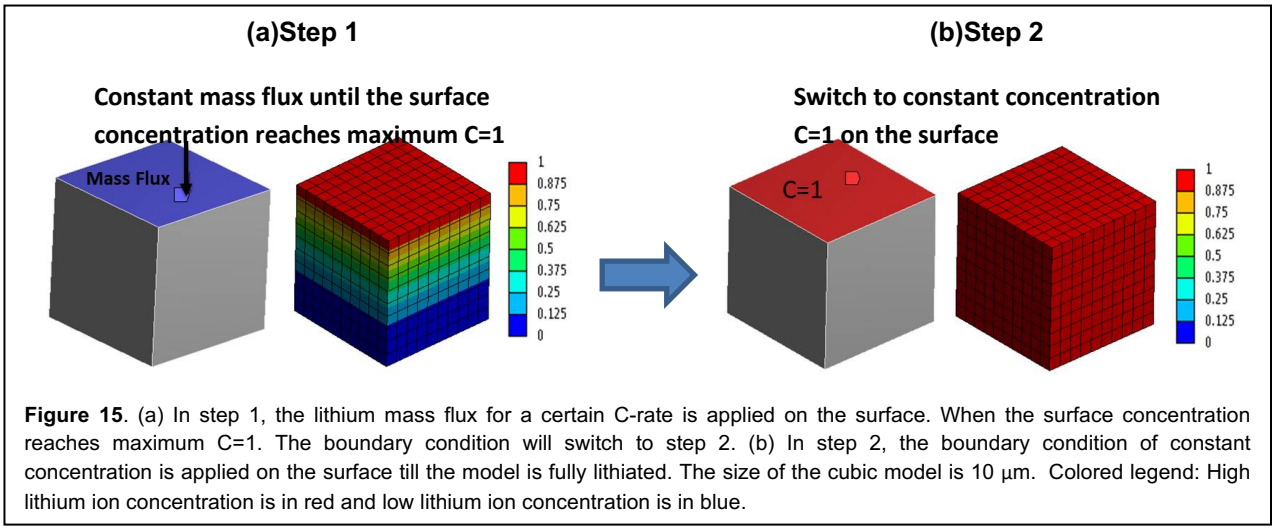

Figure 15. (a) In step 1, the lithium mass flux for a certain C-rate is applied on the surface. When the surface concentration reaches maximum C=1. The boundary condition will switch to step 2. (b) In step 2, the boundary condition of constant concentration is applied on the surface till the model is fully lithiated. The size of the cubic model is 10 μm. Colored legend: High lithium ion concentration is in red and low lithium ion concentration is in blue.

Figure 16 shows the concentration profiles along the direction of lithium diffusion in the model for different C-rates. It is observed that higher C-rates result in higher concentration gradients near the material surface during the initial lithiation (**Figure 16a**). If we compare the concentration profiles at the time when the surface reaches 100% lithiation for each C-rate, it could be observed that higher C-rates cause larger concentration differences throughout the material (**Figure 16b**). A larger concentration gradient might cause a larger stress during the lithium intercalation process. The lithium concentration profiles, normal stresses, shear stresses, elastic strain energy at different C-rates (1C, 2C, 6C and 10C) will be compared and discussed.

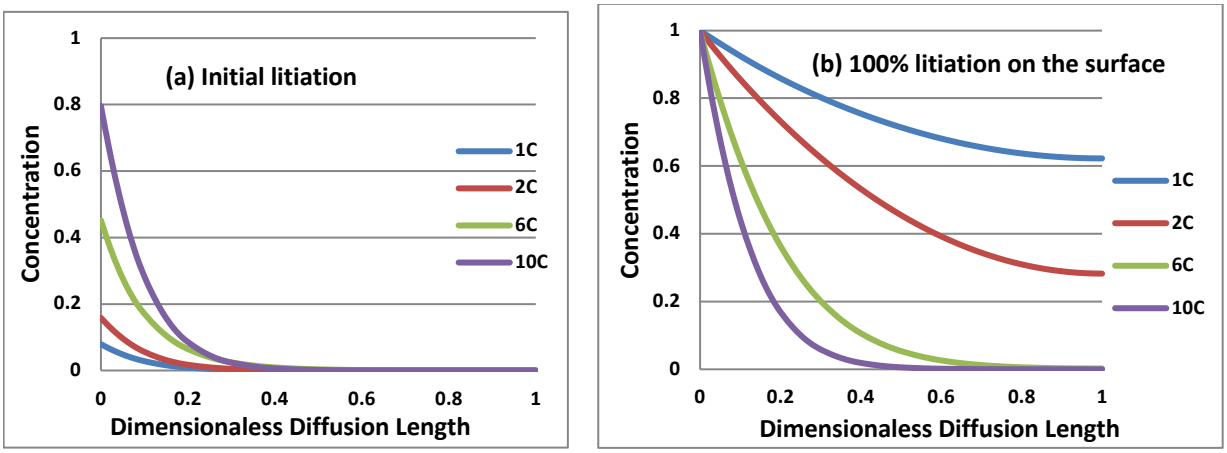

Figure 16. (a) Initial lithiation on the surface of different C-rates. Higher C-rates result in higher concentration gradients near the material surface. (b) Concentration profiles when the surface reaches 100% lithiation. Higher C-rates cause larger concentration differences throughout the material.

Upon completion of **Objective 2**, we will provide quantitative data of lithium concentration profiles and stress evolution for different C-rates. The maximum stress and minimum stress at different lithiation stages will also be compared. Results from **Objective 2** will provide a better understanding of stress evolution inside materials for different C-rates and explain why higher C-rate might result in a higher internal stress, causing the particle fracture and capacity loss.

References

[1] Office of Atmospheric Programs, 2010, "EPA Analysis of the American Power Act," U.S. Environmental Protection Agency.

[2] Environmental Protection Agency and Department of Transportation, 2011, "2017–2025 Model Year Light-Duty Vehicle Greenhouse Gas Emissions and Corporate Average Fuel Economy Standards," Federal Register, **76**(153) .

[3] Chiang, Y., 2010, "Building a Better Battery," Science, **330**(6010) pp. 1485-1486.

[4] Kang, B., and Ceder, G., 2009, "Battery Materials for Ultrafast Charging and Discharging," Nature, **458**(7235) pp. 190-193.

[5] Zhang, Y., Wang, C., and Tang, X., 2011, "Cycling Degradation of an Automotive LiFePO(4) Lithium-Ion Battery," Journal of Power Sources, **196**(3) pp. 1513-1520.

[6] Chen, G. Y., Song, X. Y., and Richardson, T. J., 2006, "Electron Microscopy Study of the LiFePO4 to FePO4 Phase Transition," Electrochemical and Solid State Letters, **9**(6) pp. A295-A298.

[7] Zhao, K., Pharr, M., Vlassak, J. J., 2010, "Fracture of Electrodes in Lithium-Ion Batteries Caused by Fast Charging," Journal of Applied Physics, **108**(7) pp. 073517.

[8] Gabrisch, H., Wilcox, J., and Doeff, M. M., 2008, "TEM Study of Fracturing in Spherical and Plate-Like LiFePO4 Particles," Electrochemical and Solid State Letters, **11**(3) pp. A25-A29.

[9] U.S. Energy Information Administration, 2012, "April 2012 Monthly Energy Review," U.S. Department of Energy, DOE/EIA-0035, Washington, D.C.

[10] S. C. Davis, S. W. Diegel, R. G. Boundy, 2011, "Transportation Energy Data Book 30th Edition," U.S. Department of Energy, Washington, DC.

[11] Yuan, L., Wang, Z., Zhang, W., 2011, "Development and Challenges of LiFePO4 Cathode Material for Lithium-Ion Batteries," Energy & Environmental Science, **4**(2) pp. 269-284.

[12] Park, M., Zhang, X., Chung, M., 2010, "A Review of Conduction Phenomena in Li-Ion Batteries," Journal of Power Sources, **195**(24) pp. 7904-7929.

[13] Chung, S., Bloking, J., and Chiang, Y., 2002, "Electronically Conductive Phospho-Olivines as Lithium Storage Electrodes," Nature Materials, **1**(2) pp. 123-128.

[14] Chung, S., Bloking, J., and Chiang, Y., 2003, "From our Readers - on the Electronic Conductivity of Phosphoolivines as Lithium Storage Electrodes - Reply," Nature Materials, **2**(11) pp. 702-703.

[15] Zhang, W., 2011, "Structure and Performance of LiFePO(4) Cathode Materials: A Review," Journal of Power Sources, **196**(6) pp. 2962-2970.

[16] Meethong, N., Kao, Y., Tang, M., 2008, "Electrochemically Induced Phase Transformation in Nanoscale Olivines Li1-xMPO4 (M = Fe, Mn)," Chemistry of Materials, **20**(19) pp. 6189-6198.

[17] Meethong, N., Huang, H. S., Carter, W. C., 2007, "Size-Dependent Lithium Miscibility Gap in Nanoscale Li1-xFePO4," Electrochemical and Solid State Letters, **10**(5) pp. A134-A138.

[18] Meethong, N., Huang, H. S., Speakman, S. A., 2007, "Strain Accommodation during Phase Transformations in Olivine-Based Cathodes as a Materials Selection Criterion for High-Power Rechargeable Batteries," Advanced Functional Materials, **17**(7) pp. 1115-1123.

[19] Kao, Y., Tang, M., Meethong, N., 2010, "Overpotential-Dependent Phase Transformation Pathways in Lithium Iron Phosphate Battery Electrodes," Chemistry of Materials, **22**(21) pp. 5845-5855.

[20] Meethong, N., Kao, Y., Speakman, S. A., 2009, "Aliovalent Substitutions in Olivine Lithium Iron Phosphate and Impact on Structure and Properties," Advanced Functional Materials, **19**(7) pp. 1060-1070.

[21] Rousse, G., Rodriguez-Carvajal, J., Patoux, S., 2003, "Magnetic Structures of the Triphylite LiFePO(4) and of its Delithiated Form FePO(4)," Chemistry of Materials, **15**(21) pp. 4082-4090.

[22] Boulfelfel, S. E., Seifert, G., and Leoni, S., 2011, "Atomistic Investigation of Li+ Diffusion Pathways in the Olivine LiFePO4 Cathode Material," Journal of Materials Chemistry, **21**(41) pp. 16365-16372.

[23] Nishimura, S., Kobayashi, G., Ohoyama, K., 2008, "Experimental Visualization of Lithium Diffusion in Li(x)FePO(4) RID B-2754-2011 RID A-4920-2011," Nature Materials, **7**(9) pp. 707-711.

[24] Malik, R., Burch, D., Bazant, M., 2010, "Particle Size Dependence of the Ionic Diffusivity," Nano Letters, **10**(10) pp. 4123-4127.

[25] Dathar, G. K. P., Sheppard, D., Stevenson, K. J., 2011, "Calculations of Li-Ion Diffusion in Olivine Phosphates," Chemistry of Materials, **23**(17) pp. 4032-4037.

[26] Yang, J., and Tse, J. S., 2011, "Li Ion Diffusion Mechanisms in LiFePO(4): An Ab Initio Molecular Dynamics Study," Journal of Physical Chemistry a, **115**(45) pp. 13045-13049.

[27] Laffont, L., Delacourt, C., Gibot, P., 2006, "Study of the LiFePO4/FePO4 Two-Phase System by High-Resolution Electron Energy Loss Spectroscopy," Chemistry of Materials, **18**(23) pp. 5520-5529.

[28] Delmas, C., Maccario, M., Croguennec, L., 2008, "Lithium Deintercalation in LiFePO(4) Nanoparticles Via a Domino-Cascade Model RID G-6492-2011," Nature Materials, **7**(8) pp. 665-671.

[29] Brunetti, G., Robert, D., Bayle-Guillemaud, P., 2011, "Confirmation of the Domino-Cascade Model by LiFePO4/FePO4 Precession Electron Diffraction," Chemistry of Materials, **23**(20) pp. 4515-4524.

[30] Tang, M., Carter, W. C., and Chiang, Y., 2010, "Electrochemically Driven Phase Transitions in Insertion Electrodes Or Lithium-Ion Batteries: Examples in Lithium Metal Phosphate Olivines," Annual Review of Materials Research, Vol 40, **40**pp. 501-529.

[31] Tang, M., Huang, H. -., Meethong, N., 2009, "Model for the Particle Size, Overpotential, and Strain Dependence of Phase Transition Pathways in Storage Electrodes: Application to Nanoscale Olivines," Chemistry of Materials, **21**(8) pp. 1557-1571.

[32] Van der Ven, A., Garikipati, K., Kim, S., 2009, "The Role of Coherency Strains on Phase Stability in Li(x)FePO(4): Needle Crystallites Minimize Coherency Strain and Overpotential," Journal of the Electrochemical Society, **156**(11) pp. A949-A957.

[33] Bai, P., Cogswell, D. A., and Bazant, M. Z., 2011, "Suppression of Phase Separation in LiFePO(4) Nanoparticles during Battery Discharge," Nano Letters, **11**(11) pp. 4890-4896.

[34] Cogswell, D. A., and Bazant, M. Z., 2012, "Coherency Strain and the Kinetics of Phase Separation in LiFePO4 Nanoparticles," Acs Nano, **6**(3) pp. 2215-2225.

[35] Dreyer, W., Jamnik, J., Guhlke, C., 2010, "The Thermodynamic Origin of Hysteresis in Insertion Batteries," Nature Materials, **9**(5) pp. 448-453.

[36] Dreyer, W., Guhlke, C., and Huth, R., 2011, "The Behavior of a Many-Particle Electrode in a Lithium-Ion Battery," Physica D-Nonlinear Phenomena, **240**(12) pp. 1008-1019.

[37] Malik, R., Zhou, F., and Ceder, G., 2011, "Kinetics of Non-Equilibrium Lithium Incorporation in LiFePO(4)," Nature Materials, **10**(8) pp. 587-590.

[38] Belu, A., Graham, D., and Castner, D., 2003, "Time-of-Flight Secondary Ion Mass Spectrometry: Techniques and Applications for the Characterization of Biomaterial Surfaces," Biomaterials, **24**(21) pp. 3635-3653.

[39] Martin, J. F., Yamada, A., Kobayashi, G., 2008, "Air Exposure Effect on LiFePO4," Electrochemical and Solid State Letters, **11**(1) pp. A12-A16.

[40] Wang, D., Wu, X., Wang, Z., 2005, "Cracking Causing Cyclic Instability of LiFePO4 Cathode Material," Journal of Power Sources, **140**(1) pp. 125-128.

[41] C.K ChiuHuang, S. Y. S. H., 2013, "Stress Evolution on the Phase Boundary in LiFePO4 Particles," Journal of the Electrochemical Society, **160**(11) pp. A2184-A2188.

[42] Deshpande, R., Qi, Y., and Cheng, Y., 2010, "Effects of Concentration-Dependent Elastic Modulus on Diffusion-Induced Stresses for Battery Applications," Journal of the Electrochemical Society, **157**(8) pp. A967-A971.

[43] Maxisch, T., and Ceder, G., 2006, "Elastic Properties of Olivine LixFePO4 from First Principles," Physical Review B, **73**(17) pp. 174112.

[44] Christensen, J., and Newman, J., 2006, "Stress Generation and Fracture in Lithium Insertion Materials RID A-5481-2008 RID B-8650-2008," Journal of Solid State Electrochemistry, **10**(5) pp. 293-319.

[45] Zhang, X., Sastry, A. M., and Shyy, W., 2008, "Intercalation-Induced Stress and Heat Generation within Single Lithium-Ion Battery Cathode Particles," Journal of the Electrochemical Society, **155**(7) pp. A542-A552.

[46] Cheng, Y., and Verbrugge, M. W., 2009, "Evolution of Stress within a Spherical Insertion Electrode Particle Under Potentiostatic and Galvanostatic Operation," Journal of Power Sources, **190**(2) pp. 453-460.

[47] Morgan, D., Van der Ven, A., and Ceder, G., 2004, "Li Conductivity in LixMPO4 (M = Mn, Fe, Co, Ni) Olivine Materials," Electrochemical and Solid State Letters, **7**(2) pp. A30-A32.

[48] Singh, G. K., Ceder, G., and Bazant, M. Z., 2008, "Intercalation Dynamics in Rechargeable Battery Materials: General Theory and Phase-Transformation Waves in LiFePO4," Electrochimica Acta, **53**(26) pp. 7599-7613.

[49] Garcia, R., Chiang, Y., Carter, W., 2005, "Microstructural Modeling and Design of Rechargeable Lithium-Ion Batteries," Journal of the Electrochemical Society, **152**(1) pp. A255-A263.